Final Technical Report

Award Numbers G13AP00044, G13AP00043

Hypocenter and Focal Mechanism Determination of the August 23, 2011 Virginia Earthquake Aftershock Sequence: Collaborative Research with VA Tech and Boston College

Martin Chapman, John Ebel, Qimin Wu and Stephen Hilfiker

Department of Geosciences
Virginia Polytechnic Institute and State University
4044 Derring Hall
Blacksburg, Virginia, 24061 (MC, QW)

Department of Earth and Environmental Sciences
Boston College
Devlin Hall 213
140 Commonwealth Avenue
Chestnut Hill, Massachusetts 02467 (JE, SH)

Phone (Chapman): (540) 231-5036
Fax (Chapman): (540) 231-3386
Phone (Ebel): (617) 552-8300
Fax (Ebel): (617) 552-8388
Email: mcc@vt.edu (Chapman), ebel@bc.edu (Ebel), wqimin86@vt.edu (Wu), hilfiker@bc.edu (Hilfiker)

Project Period: July 2013 - December, 2014

Abstract

The aftershocks of the M_w 5.7, August 23, 2011 Mineral, Virginia, earthquake were recorded by 36 temporary stations installed by several institutions. We located 3,960 aftershocks from August 25, 2011 through December 31, 2011. A subset of 1,666 aftershocks resolves details of the hypocenter distribution. We determined 393 focal mechanism solutions.

Aftershocks near the mainshock define a previously recognized tabular cluster with orientation similar to a mainshock nodal plane; other aftershocks occurred 10-20 kilometers to the northeast. Detailed relocation of events in the main tabular cluster, and hundreds of focal mechanisms, indicate that it is not a single extensive fault, but instead is comprised of at least three and probably many more faults with variable orientation.

A large percentage of the aftershocks occurred in regions of positive Coulomb static stress change and approximately 80% of the focal mechanism nodal planes were brought closer to failure. However, the aftershock distribution near the mainshock appears to have been influenced strongly by rupture directivity. Aftershocks at depths less than 4 km, near the mainshock and 10-20 km to the northeast, exhibit reverse mechanisms with N-NW trending nodal planes, indicating N80˚E trending, sub-horizontal, maximum compressive stress. Most focal mechanisms at depths greater than 6 km are similar to the mainshock, with N-NE trending nodal planes: together with the mainshock they indicate a more E-SE (approximately N100˚E) trending, sub-horizontal maximum compressive stress. A concentration of aftershocks in the 4-6 km depth range near the mainshock are mostly of reverse type, but display a 90-degree range of nodal plane trend. Those events appear to outline the periphery of mainshock rupture. The focal mechanisms of aftershocks at depths less than 4 km and those at depths greater than 6, along with the mainshock, point to the possibility of a depth-dependent stress field prior to the occurrence of the mainshock.

Introduction

The Mineral, Virginia, earthquake occurred at 17:51:3.9 UTC on August 23, 2011, with epicenter at 37.905°N, 77.975°W and focal depth 8 km (Chapman, 2013). It caused structural damage consistent with level VIII of the modified Mercalli intensity scale near the epicenter in Louisa County, Virginia, and significant damage as far away as Washington, D.C. (Horton *et al*., 2015a; Heller and Carter, 2015; Wells *et al*., 2015). The USGS/St. Louis University moment tensor solution (Herrmann, 2011) indicates moment magnitude M_w 5.65, and a nodal plane with strike N28°E, dip 50° and rake 113°, in agreement with aftershock locations (Herrmann, 2011; Chapman, 2013; McNamara *et al.*, 2014; Horton *et al.*, 2015b). This reverse-fault earthquake occurred in an area known as the central Virginia seismic zone (CVSZ), which has a long history of moderate earthquake activity (Taber, 1913; Bollinger, 1969, 1973a, 1973b; Kim and Chapman, 2005; Chapman, 2013; Chapman, 2015; Horton *et al.*, 2015a, and references therein). Geological structure in the CVSZ is dominated by thin-skinned Appalachian thrusting. The earthquakes occur within crystalline rocks of Paleozoic age, above the basal Appalachian detachment inferred from seismic reflection profiles in the area (Coruh et al., 1988; Pratt et al., 1988; Bollinger et al., 1991). The area was subjected to extensional stresses in the Mesozoic. However, the seismicity is not correlated with mapped faults or with structure imaged on reflection profiles (Pratt et al., 2015).

The mainshock was a complex rupture comprised of multiple subevents in a small fault area centered at depths between approximately 6.0 and 8.0 km (Chapman, 2013; Hartzell *et. al*.,

2013, Motazedian and Ma, 2014). Previous studies found that the aftershocks occurred mostly within a tabular zone exhibiting strike and dip similar to a mainshock focal mechanism nodal plane (Herrmann, 2011; Chapman, 2013; McNamara *et al.*, 2014; Wu *et al.*, 2014; Horton *et al*., 2015b). Previous studies also identified some aftershocks approximately 10-20 km to the east and northeast of the mainshock that were interpreted to be triggered by stress transfer due to the mainshock (McNamara *et al*., 2014; Wu *et al*., 2014; Horton *et al*., 2015b). The previously determined regional moment tensor (RMT) solutions for 16 of the largest aftershocks show a diversity of nodal plane orientation, although most of them are of reverse type (Herrmann, 2011; McNamara *et al*., 2014).

Here, we describe a study of the aftershock sequence of the Mineral earthquake using a larger data set than was used previously. The purpose was to better understand the nature of faulting in the area, in particular, the stress regime driving the still on-going (early 2015) aftershock activity. We focused on details of the hypocenter locations of thousands of aftershocks, focal mechanisms of several hundred aftershocks, and the dominant role that stress transfer appears to play in the aftershock process of the Mineral earthquake. Presumably, the aftershock process of this event is representative of other moderate to large shocks that have occurred and will occur in eastern North America, and a better understanding of the Mineral event could shed more light on the state of stress in intraplate North America.

Data and Analysis

Aftershock Locations

Shortly after the mainshock, teams from Virginia Tech, University of Memphis, Lehigh University, Incorporated Research Institutions for Seismology (IRIS) and the United States Geological Survey (USGS) deployed seismic instruments and recorded a dataset that is archived at the IRIS Data Management Center (http://www.iris.edu/dms/dmc/). Figure 1 shows the locations of the 32 temporary stations used in this study. We used the entire available data set recorded from August 25, 2011 through December 31, 2011, when the seismicity rate was high and location capability was maximum and stable. We applied a detection algorithm that combined the short-term average and long-term average ratio (STA/LTA) method (Allen, 1982; Withers *et al*., 1998) with a cross-correlation method that scanned through the continuous waveform recordings with signal templates to detect as many events as possible. The cross-correlation method refined the STA/LTA detections by removing many false triggers and detected additional small events. The automatic detections were visually reviewed. This resulted in 3,960 aftershocks detected within the 129 day time range of our study.

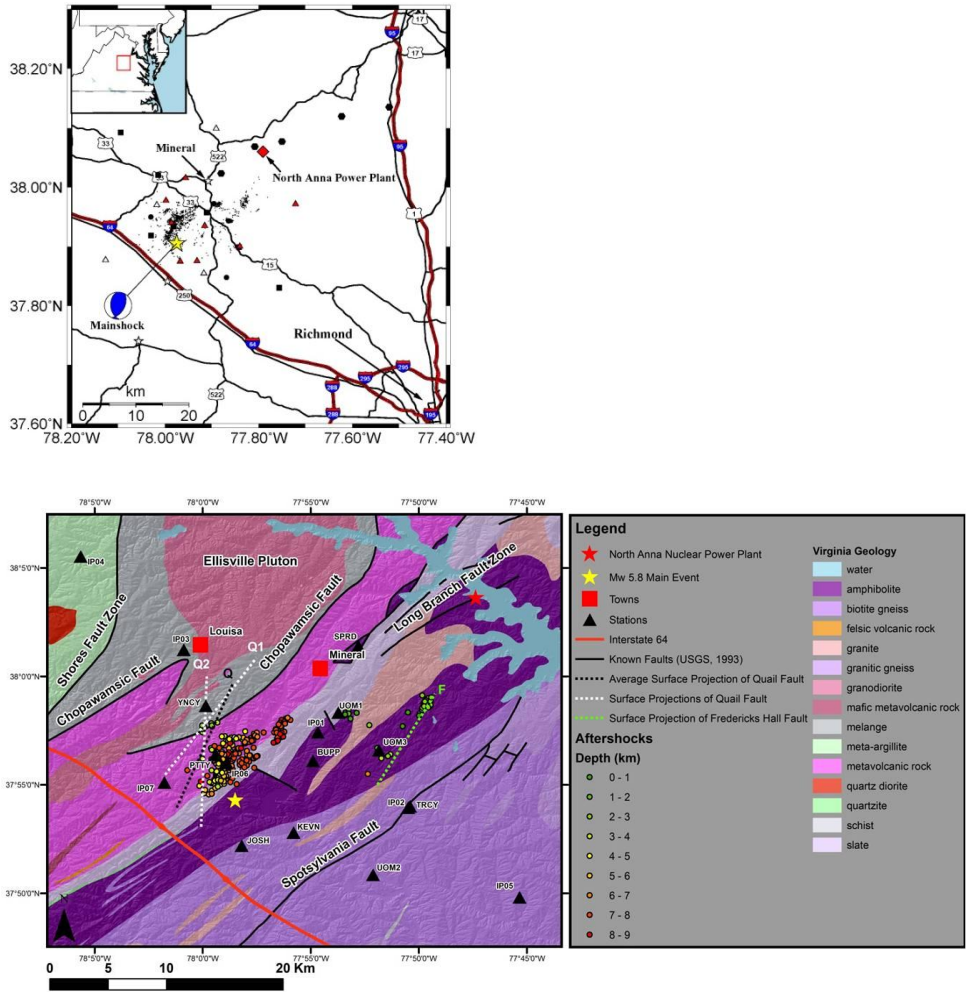

Figure 1. (Top) Map showing aftershock locations and seismic stations for the period late August, 2011 through December, 2011. Different symbols show different seismic network stations archived at the IRIS DMC. The focal mechanism is from Herrmann (2011). (Bottom) Map view showing only relative hypocenters with a location uncertainty of one standard deviation (σ) < 0.1 km. Simplified Virginia geology from Dicken et al., (2005) is shown with Lidar DEM. Dashed lines indicate surface projections of potential faults resolved by aftershock relocation. The strike and dip of the planes used to project Q1, Q2, and Q are 045º/67º, 002º/72º, and 025º/68º, respectively. The strike and dip of the plane used to project F are 033º/85º. Virginia fault, geology, and DEM data were sourced from the USGS.

A total of 3,018 earthquakes were located initially using the single-event location program HYPOELLIPSE (Lahr, 1999). The data set we used for further analysis involved 1,666 particularly well-constrained events with at least 10 arrival time picks and a root-mean-square (RMS) travel-time residual less than 0.1 s. The 1-D velocity model used here is based on the velocity model routinely used for hypocenter location in central Virginia by the Virginia Tech Seismological Observatory (Bollinger *et al*., 1980). That model was further refined by analyzing aftershocks of the Mineral earthquake (Chapman, 2013). The velocity model consists of three layers. The upper crust is represented by a 15-km-thick layer with *P*- and *S*-wave velocities of 5.96 km/s and 3.53 km/s respectively. The lower crust has a *P*-wave velocity of 6.50 km/s, *S*-

wave velocity of 3.79 km/s and a thickness of 21 km. Below the Moho, the half-space *P*-wave and *S*-wave velocities are 8.18 km/s and 4.73 km/s, respectively.

Relative Event Locations in the Main Aftershock Zone

We applied double-difference techniques to relocate the aftershocks. We used two approaches**.** In the first approach, we used manual P and S-wave arrival time picks and the algorithm HypoDD (Waldhauser and Ellsworth, 2000; Waldhauser, 2001). Waveform cross-correlation was used in the second approach. Double difference aftershock relocations from the first approach are shown in Figure 2 in map and profile views. The error estimates reported by HypoDD for both horizontal and vertical directions are tens of meters. The double difference locations do not significantly differ from the initial locations in terms of horizontal location. However, many events that were initially located near the surface were relocated to greater depth. The initial single-event locations have an average depth of 4.01 km (median 4.43 km); in comparison, the average depth determined by HypoDD is 4.42 km (median 4.50 km). In map view (Figure 2) the aftershocks within 10 km of the mainshock lie in a northeast-trending cluster which, in 3-dimensions, forms a southeast-dipping tabular zone with general orientation closely similar to that of a mainshock focal mechanism nodal plane. Below, we refer to these events as the main cluster. However, many aftershocks occurred further to the east and northeast of the mainshock, in several small clusters, mostly located 10 - 20 kilometers from the main cluster. Below, we refer to the more distant aftershocks to the east and northeast of the main cluster as the northeastern aftershocks.

The main aftershock cluster is approximately 1 km thick and exhibits gross strike and dip in agreement with the mainshock fault plane (Figure 2, red symbols, profile A-A').This led many researchers to initially assume that the aftershocks illuminate a single extensive fault (Quail fault) that ruptured in the mainshock (Horton et al., 2012a, 2012b, 2015). But that is not the case. The results of our application of the first location approach, wherein all the main aftershock events are relocated as one cluster using HypoDD, indicates that the great majority of the earthquakes in the main aftershock cluster lie between 4 and 6 km, at shallower depth and well to the northeast of the mainshock rupture (Chapman 2013). One interpretation is that those aftershocks mark the periphery of the rupture and form a quarter-circle arc or halo above the shallow part of the rupture zone, in the direction of rupture propagation (Chapman, 2013). Application of the second relocation approach suggests the possibility of 3 planar arrangements of aftershocks, suggesting at least 3 faults in the main aftershock cluster. As we discuss in later sections of this report, the near-planar arrangement of the aftershocks in the main cluster belies the fact that focal mechanism solutions of the majority of them exhibit nodal planes with orientations significantly different from the mainshock. Another important observation made possible by the extensive set of focal mechanism we have determined is the fact that this variability of the main cluster focal mechanisms is definitely not random, but depends on the location of the aftershocks with respect to the mainshock.

The second location approach follows the technique outlined in Ebel et al. (2008). Waveform cross-correlation was used to determine precise arrival-time differences of body waves for the master event and a secondary event at common stations surrounding the epicentral area. The differences in the P and S travel times for two events at a common set of stations were used to calculate the offset in hypocentral location of the secondary event relative to the master event (Waldhauser and Ellsworth, 2000).

A jackknife analysis was used to calculate uncertainties in the relative location parameters. Stations that contributed to the relative location uncertainty were also identified as part of the jackknife analysis. When the root mean square (RMS) error between the predicted and computed relative arrival times has been reduced to less than two times the sampling period of most stations (0.02 s), no further resolution of the relative location of the hypocenter is possible. Thus, the smallest uncertainties in the relative location hypocenters is about 120 m assuming a digital sampling period of 0.01 s and a P-wave velocity of 6.09 km/s.

The relative location analysis was carried out for a number of secondary events that have hypocenters with absolute locations near the master event to calculate the relative locations of a "cluster" of events around the master event. Multiple master events with absolute locations in different parts of the aftershock zone were used due to the large spatial extent of the seismicity following the mainshock in order to increase the probability of finding low-uncertainty relative locations for the nearby secondary events. This method improves the locations of secondary event hypocenters relative to the location of the corresponding master event, allowing for a focused analysis of the geometry of the seismogenic structure on different parts of the aftershock zone. The drawback of the method is that it does not improve the absolute location of the subsurface fault structure as a whole. In order to better constrain the relative locations of two different but nearby clusters of events for which relative locations had been calculated, a secondary event from the edge of each relative location cluster and close to the other cluster was selected, and the relative locations of these two secondary events was calculated. The result of this calculation allowed the relative locations of the two clusters to be precisely computed.

Several assumptions were made in the application of the relative-location method of Ebel et al. (2008). The master and secondary events are assumed to have similar focal mechanisms, implying that the P and S waves that arrive at each station for the two events take off from similar locations on the body wave radiation patterns from each source. Ray paths from the master event and secondary event to a common station are assumed to be similar, and thus the waveforms from both events would experience the same scattering and frequency attenuation when recorded at a given station. The velocity structure in the hypocentral region that encompasses both the master and secondary events is assumed to be uniform, and any minor deviations in the ray paths to a given station for the two events cause only small differences in the waveforms of the two events given the station sampling frequency of 100 or 200 Hz.

The second (master event) approach used a subset of 1600 events shown in Figure 3. Multiple "clusters" were created that contained one master event and tens to hundreds of possible secondary events for use in the relative location analysis (Figure 3). A two-layer crustal velocity model developed for the Central Virginia Seismic Zone (CVSZ) (Bollinger et al., 1980; Chapman, 2013) was used to determine the relative hypocenter locations.

As noted above, due to the relatively large spatial extent of seismicity both along strike and down dip on the main aftershock zone, multiple clusters, each with one master event and surrounding secondary events, were formed, and a separate relative location analysis was carried out for the events in each cluster (Figure 3). The purpose of this was to maximize the chances that high-precision relative locations could be computed. An event near the center of each cluster that had a high signal-to-noise ratio and was well-recorded on as many stations as possible was chosen as the master event (Figure 3). The secondary events in a cluster were individually analyzed with the master event to determine if an accurate relative location of the secondary event relative to the master event could be calculated. For each master event-secondary event

pair that was analyzed, a second-order zero-phase infinite impulse response filter (2-10 Hz passband) was used to filter the signals before processing in the relative location analysis. Time

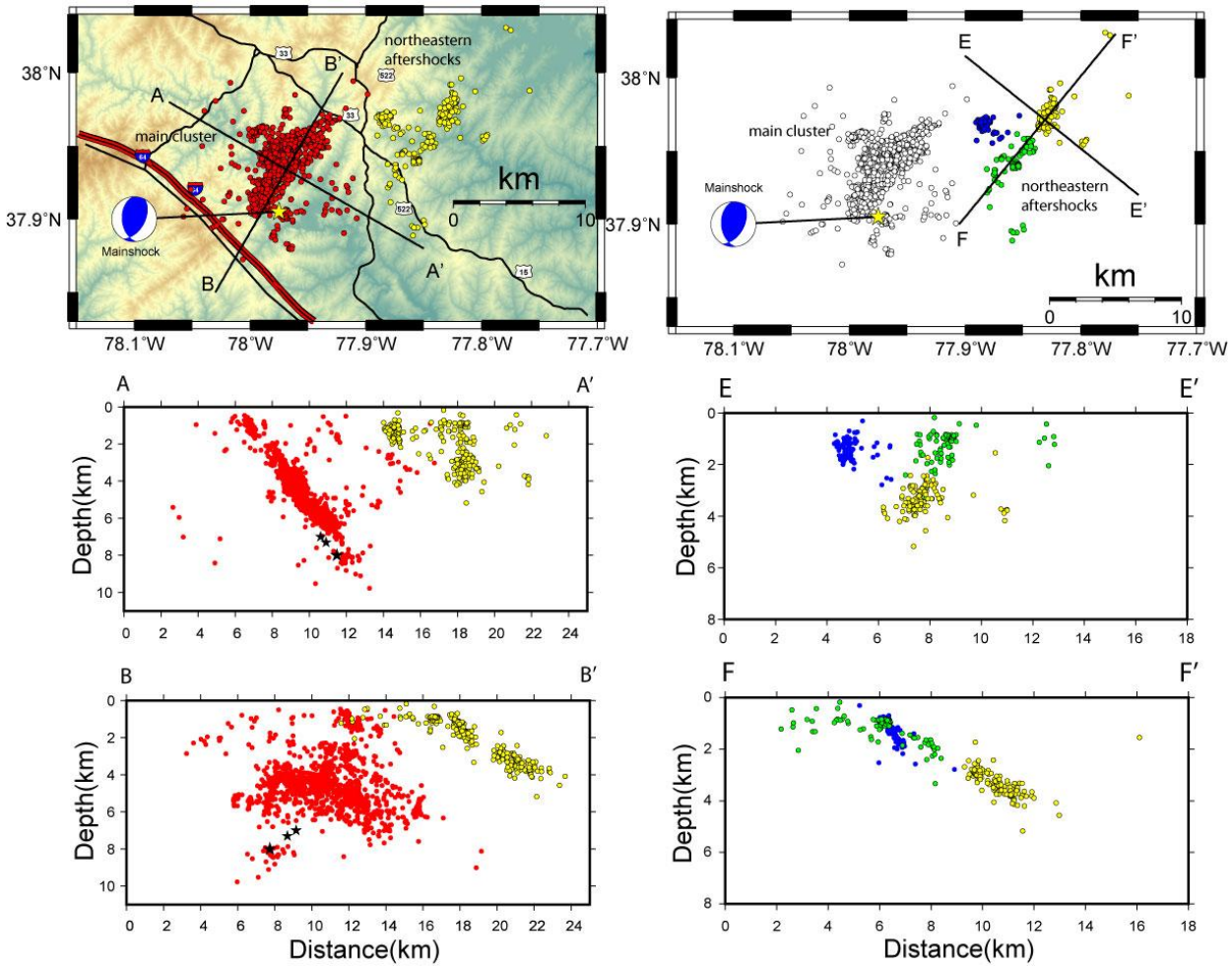

Figure 2. Map and profile views of aftershock hypocenters. Red circles show aftershocks in the main cluster, yellow, blue and green circles show aftershocks in the northeastern cluster. The three black stars indicate the hypocenters of the subevents comprising the mainshock (Chapman, 2013).

windows encompassing the arrival times of the P waves (0.1s before to 0.3s after the hand-picked P-wave arrival) on the vertical component and S waves (0.5s before to 1.5s after the hand-picked S-wave arrival) on all three components were created for the master event and the secondary event. These time windows were used in a cross-correlation to find the time shift with the maximum similarity between the master event and secondary event P and S waveforms at a common station (Figure 4). Normalized cross-correlation coefficients (C-values) greater than 0.6 were determined to represent cross-correlations with a high degree of similarity between waveforms, and therefore cross-correlations of body waves at a common station with C-values less than 0.6 were not used to calculate relative locations (Figure 4). Of the three station components for which S-wave cross-correlations were performed, the component with the largest C-value > 0.6 was used to calculate the S-wave arrival time difference between the master event and the secondary event (Figure 5).

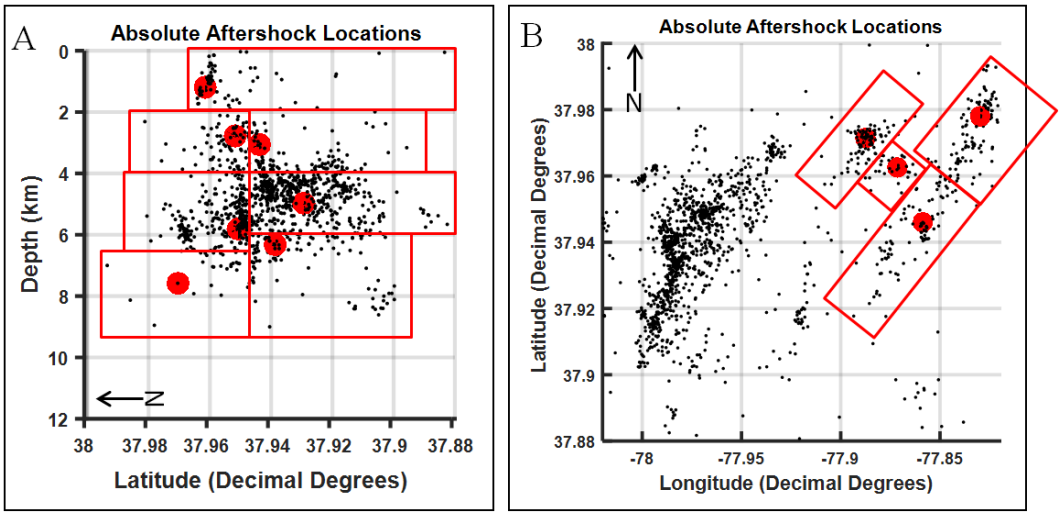

Figure 3. (A) Cross-sectional view of the absolute aftershock locations in the main aftershock cluster looking east. (B) Map-view showing both the main aftershock cluster and the northeastern aftershock cluster. Each red box indicates the area from which secondary events that were relocated relative to a particular master event (red circles) were selected.

Some secondary event waveforms showed similar shapes but with opposite polarities compared to the master event waveforms, resulting in large negative C-values determined in the cross-correlations. For this reason, the maximum absolute C-values were used to determine the lag time of the secondary event waveform relative to the master event waveform in order to include the opposite polarity cross-correlation results (Figure 4). In some cases, the waveforms for the master event, secondary event, or both were very sinusoidally shaped, which resulted in many cross-correlation peaks of similar values at different lag times (Figure 6). For these cases, it was unclear whether the maximum C-value represented the proper shift between the master event and secondary event even though the maximum C-value was greater than 0.6. Under these circumstances, the station and phase were not used due to this uncertainty in the correct lag time (Figure 6). The lag times associated with the maximum C-values for body wave cross-correlations at each station surrounding the events that passed the acceptance criteria described here were used to calculate the relative arrival time differences for the relative location analysis.

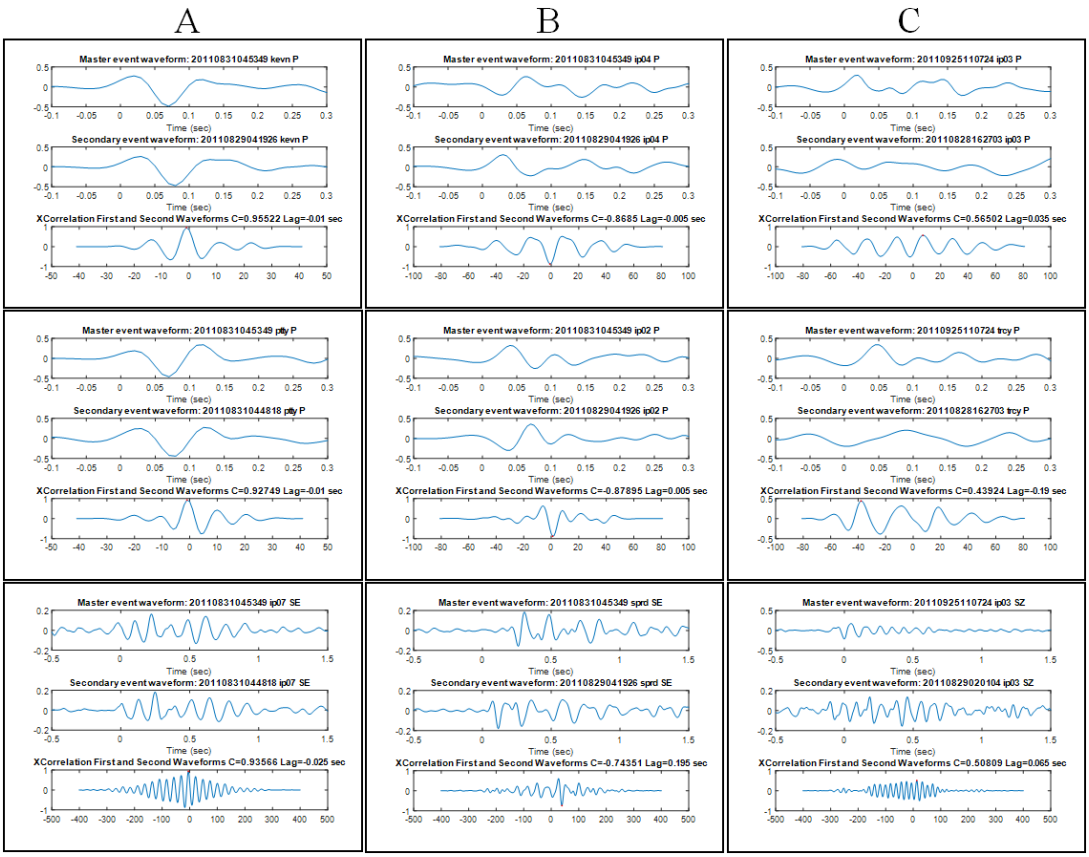

Figure 4. Examples of cross-correlations between master and secondary events. Each subplot displays master event and secondary event waveforms from the same station and cross-correlation. C is the maximum normalized cross-correlation coefficient. Column A shows examples of high positive C-values, column B shows events with opposite polarity and high negative C-values, and column C shows events with low C-values ignoring the sign of the C value ($|C| < 0.6$).

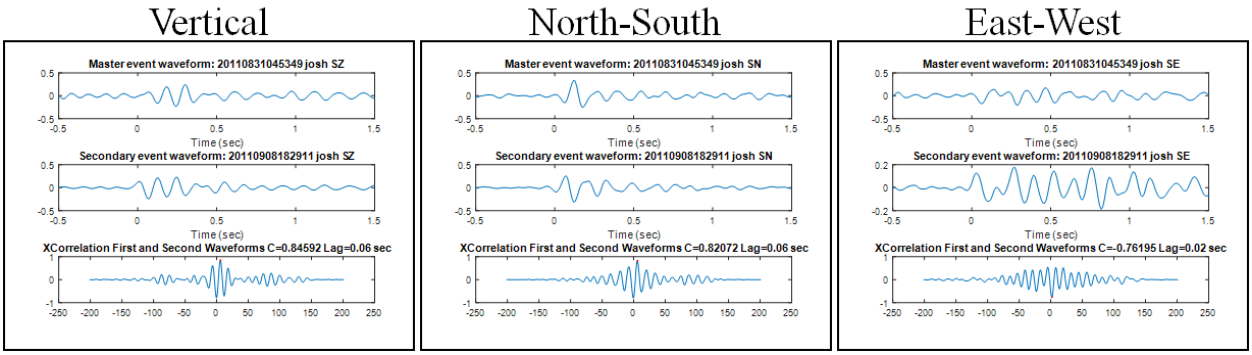

Figure 5. Cross-correlation results for S-wave at station JOSH. The cross-correlation resulted in absolute C-values > 0.6 for each component. The vertical component resulted in the largest absolute C-value for the S-wave at this station. In this case, the cross-correlation of S-waves recorded by the North-South component resulted in the same lag time as the vertical component, which added confidence that an accurate S-wave lag time had been found.

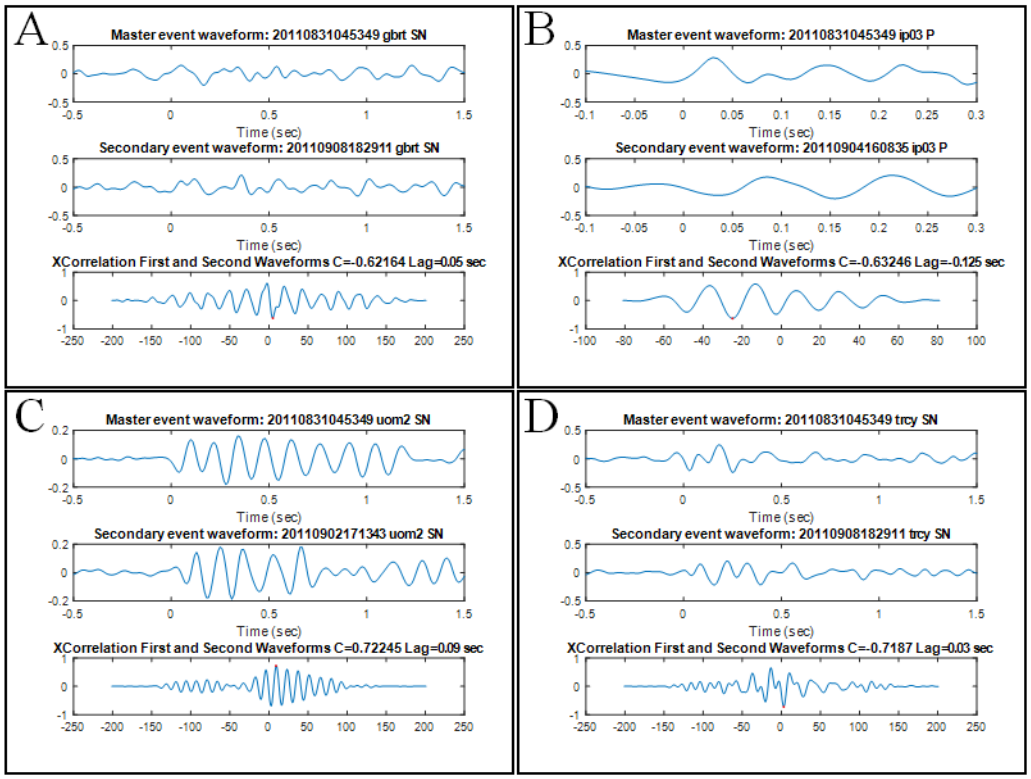

Figure 6. Examples of normalized cross-correlation coefficients (C-values) > 0.6 that were not used in the relative location analysis. Figures A-D show examples of situations where multiple lag times correspond with C-values of similar magnitudes. Figures C and D show examples of lag times that resulted in a maximum absolute C-value > 0.6 when the secondary event waveform is shifted to the right relative to the master event waveform. The appearance of the first arrivals of these waveforms suggests that there should be a negative lag time that shifts the secondary event waveform to the left relative to the master event waveform.

The relative location method summarized above was used to relocate 880 events with RMS errors for the relative locations below about 0.02 sec, which indicates that the maximum possible precision of these relative locations was achieved. Relative locations for secondary events in a cluster around individual master events were computed, and then the relative locations of pairs of events from different clusters were used to find accurate relative locations of the different clusters relative to each other. Thus, effectively every master event on the main fault structure was relocated relative to one well-defined master event using the relative location method. This produced an accurate reconstruction of the main fault structure using only one master event absolute location. The resulting relative location hypocenters revealed trends in seismicity that were not apparent from absolute hypocenter locations alone, illuminating some major seismicity lineation within the main zone of aftershocks (Figure 7). These are interpreted as two larger fault planes and one smaller fault plane, and for each of these a plane of best-fit was computed through the trend of the seismicity that is interpreted to lie along that fault plane (Figures 8 and 9). Also shown on Figure 8 is a single plane that is fit through all of the aftershocks in this primary aftershock cluster. Off-fault hypocenters near the intersection of the primary fault planes were not used in the calculation of the geometry of the primary fault planes

in Figures 8 and 9 to ensure that accurate strikes, dips, and surface projections of each interpreted plane could be determined.

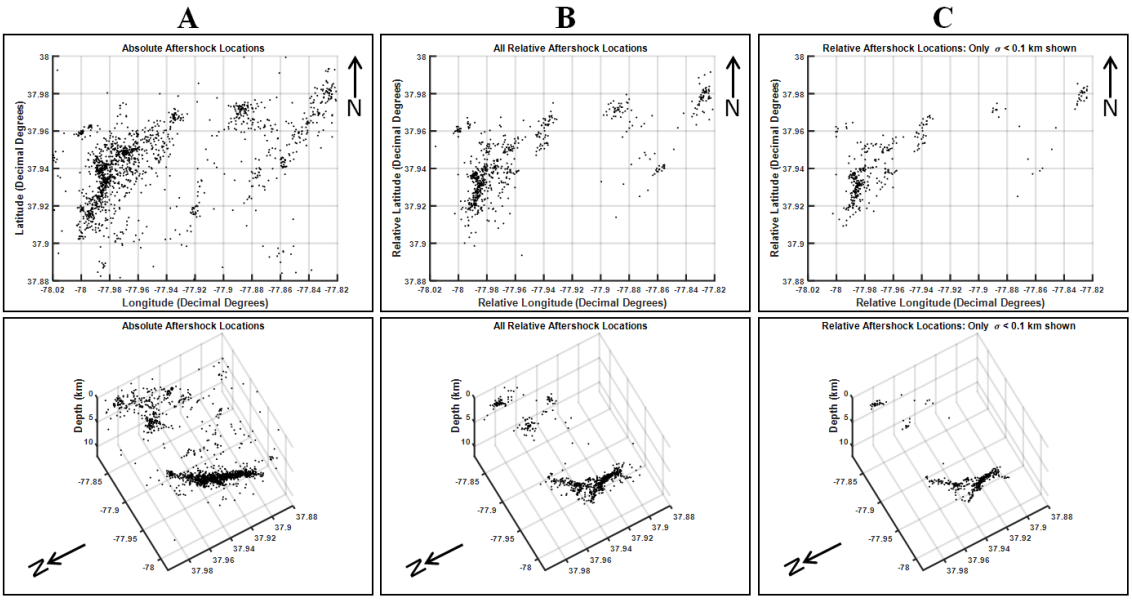

Figure 7. Comparison of absolute aftershock locations (column A), relative aftershock locations (column B), and relative aftershock locations with RMS<0.025 sec (column C).

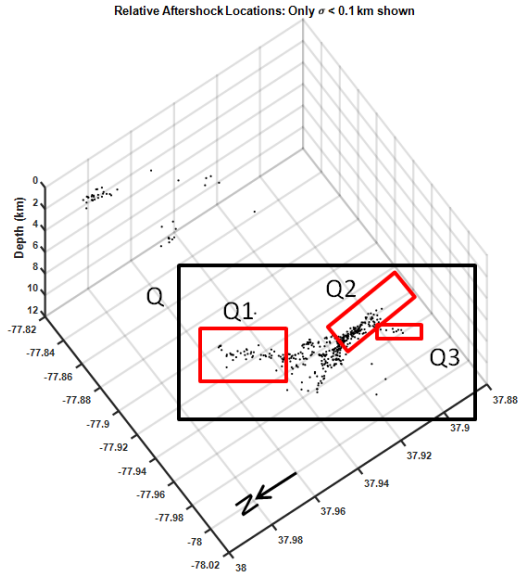

Figure 8. Major linear trends in the seismicity in the main aftershock zone (corresponding to the Quail fault initially interpreted by many investigators) are outlined by the red boxes. A plane of best-fit was created individually for Q1, Q2, and Q3. Events in box labeled Q were used to calculate a plane of best-fit to represent the main aftershock zone as a single planar feature (e.g., Quail fault). Surface projections of Q1, Q2, and Q are shown in Figure 1.

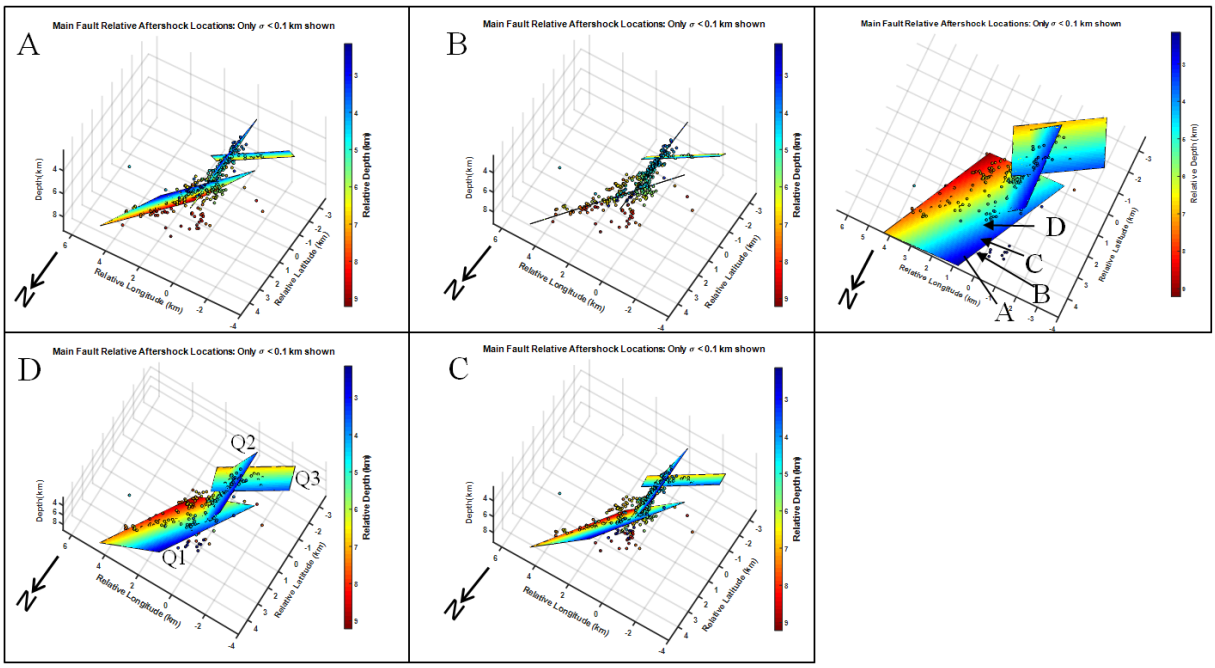

Figure 9. Oblique map views of possible fault structure in the main aftershock zone. View A shows planes Q1 and Q3 through the northwest footwall, view B is a down-dip view of the main fault planes, view C is looking down on the fault planes through the hanging wall, and view D is an oblique map view. The plot on the upper right shows vectors normal to the oblique map view represented in images A-D. Planes and hypocenters are colored by depth. The strike and dip of planes Q1, Q2, and Q3 are 045º/67º, 002º/72º, and 056º/58º, respectively.

Northeastern Aftershock Locations

Figure 2 shows clusters of aftershocks mostly between 10 and 40 km to the northeast of the main aftershock cluster (northeastern cluster, yellow, blue and green symbols). These events were initially interpreted as illuminating northeast trending, vertical faults generally parallel to Appalachian structure (Fredericks Hall Fault: Horton et al., 2015b, Wu et al., 2014).That initial interpretation must be re-assessed in view of the currently existing set of hypocenters and focal mechanisms. Our double-difference locations of the northeastern aftershocks show that these events systematically deepen to the northeast. Surprisingly, the spatial organization of the hypocenters is on northwest-trending, northeast-dipping planes (Figure 2). As described below, the focal mechanisms that we have determined for these northeastern events are consistent with the spatial organization: they suggest that the northeastern aftershocks are occurring on very consistently orientated N to NW-striking reverse faults at shallow depths (5 km or less). These active faults are not mapped, and they strike at large angles to mapped structural trends. However, their strikes parallel the trends of Mesozoic mafic dikes that are common in the area.

Focal Mechanism Determination

Two approaches were used to determine focal mechanism solutions. The first method assumes a pure double-couple moment tensor and determines the best fitting strike, dip and rake for the two nodal planes. The second approach inverts for the moment tensor, and finds the best fitting double-couple solution.

In the first approach, solutions were determined using *P*- and *SH*-wave first-motion polarities and *P*, *SH* and *SV* amplitude information derived from the 3-component records. The program FOCMEC (Snoke *et al*., 1984) was used to search through all possible fault plane solutions by comparing the observations with the predictions based on selection parameters specified by the user. The selection parameters include the number of allowed polarity errors, the range for deviations between observed and calculated amplitude ratios, and the number of ratio errors that are allowed outside that range (Snoke, 2009). Horizontal components were rotated to radial (*SV*) and transverse (*SH*) components for determining polarities and amplitude ratios. Because most of the XY and YC network stations are close to the aftershock clusters, signal-to-noise ratios were good for a large number of events. Also, the azimuthal distribution of stations shown in Figure 1 provided good constraint on focal mechanisms. The use of *SH*-wave polarity and *SH/P*, *SV/P* amplitude ratios in addition to *P*-wave polarity provided much additional constraint. The amplitudes were measured at the first peak or trough following the first-motion onset on the integrated traces. Free-surface amplitude corrections were made. The maximum number of allowed polarity errors was 4. For most events, more than 10 polarities and tens of amplitude ratios were measured.

We compared our focal mechanism solutions with all the corresponding solutions determined from regional moment tensor inversion using low-frequency waveforms (Herrmann, 2011). Figure 10 shows that in all but two cases (event numbers 1 and 11), the solutions are virtually identical, indicating that the high-frequency data from local short-period stations can indeed produce reliable mechanisms for these events. Note that event 1 occurred on August 25, 2011, when data quality was poor because of the large microseisms caused by Hurricane Irene (McNamara *et al*., 2014). Also, high-frequency polarity and amplitude data were sparse for this event due to noise levels.

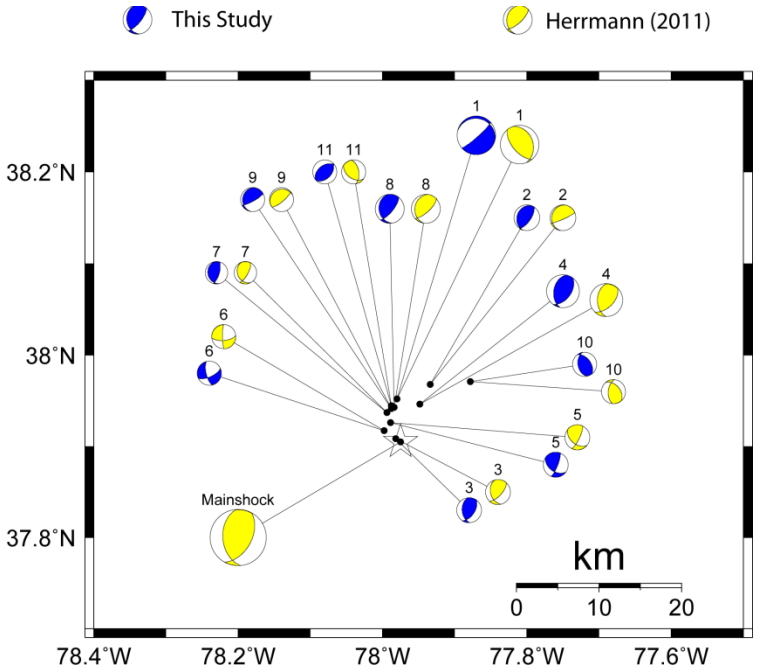

Figure 10. Comparison of focal mechanism solutions determined in this study with those derived from regional moment tensor inversion (Herrmann, 2011).

Figure 11 shows 393 focal mechanisms in map and profile view, for the main aftershock cluster and the northeastern aftershocks. Note the diversity of mechanisms in the main aftershock cluster between 4 and 6 km depth (profile B-B'). Note the highly consistent NW-striking, NE-dipping reverse mechanisms in the northeastern cluster (Profile F-F'). The solutions were classified into faulting types based on the plunge of P, T and B axes (Zoback, 1992) and listed in Table 1. The advantage of this classification is that it is based on more information than a simple classification based on rake, and is independent of the choice of fault plane. A total of 275 events are of reverse type, 35 oblique-reverse, 29 strike-slip, 12 normal and 1 oblique-normal (Table 1). Forty-one events marked as NA were not classified using the scheme, which may happen when the faulting types of the two nodal planes are different. Reverse faults dominate (70%) but all types of focal mechanism were observed. A large number of the aftershock mechanisms differ substantially from that of the mainshock. Only 54 events feature strike, dip and rake all within 20 degrees of the strike, dip and rake of the mainshock, i.e., strike: 28˚±20˚, dip: 50˚±20˚ and rake: 113˚±20˚. Based on those criteria, more than 85% of the aftershock focal mechanism solutions differ from the mainshock.

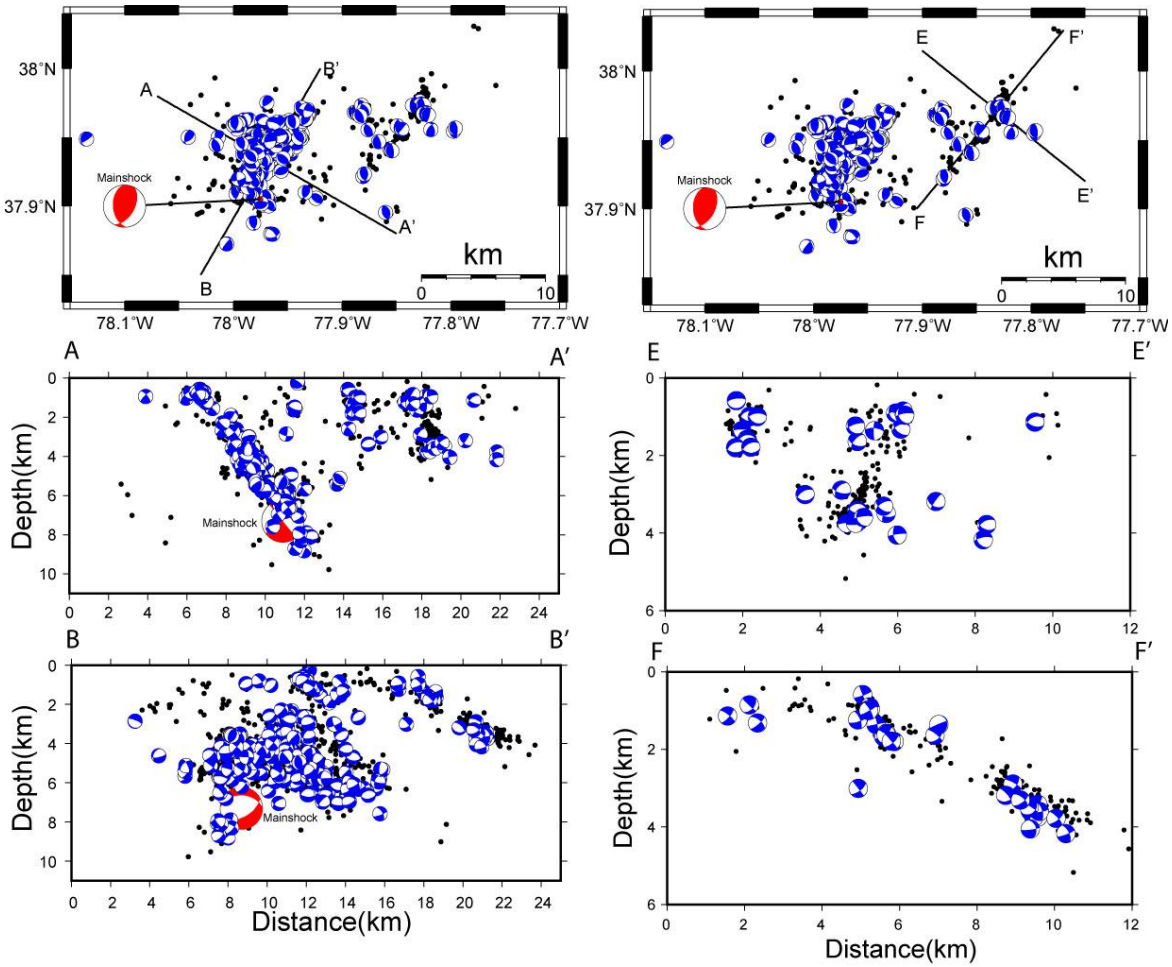

Figure 11. Focal mechanisms in the main (left) and northeastern (right) aftershock clusters. The map views show lower hemisphere projections. The profile views show projections normal to the profile.

Table 1

Types of Faulting

P-axis plunge	B-axis plunge	T-axis plunge	Type of faulting	Number of solutions
Pl > 52°		Pl < 35°	Normal	12 (3%)
40° < Pl < 52°		Pl < 20°	Normal Oblique	1 (0.3%)
Pl < 40°	Pl > 45°	Pl < 20°	Strike Slip	29 (7.4%)
Pl < 20°	Pl > 45°	Pl < 40°	Strike Slip	
Pl < 20°		40° < Pl < 52°	Reverse Oblique	35 (8.9%)
Pl < 35°		Pl > 52°	Reverse	275 (70%)
			NA	41 (10.4%)

Figure 12 plots P-axis trends of all focal mechanisms in rose diagrams to examine the distribution of solutions . The results indicate a significant variation in P-axis orientation, suggesting that aftershocks occurred on sets of fault planes with different orientations. We divided the focal-mechanism into 3 ranges of focal depth (0 - 4 km; 4 - 6 km; and > 6 km) and observed that the shallow aftershocks (depth less than 4 km) had sub-horizontal P-axis trends of approximately N70˚E. This includes events in both the main cluster and the majority of events in the northeastern group. But in the depth range from 4 to 6 km, which contains the majority of aftershocks in the main cluster and only a few in the northeastern group, three distinct sets of faults were active, one with the N70˚E P-axis trend of the shallow events, one set with P-axes mostly trending approximately N135˚E and the third with the P-axis trend of approximately N160˚E, which represents a 90 degree rotation with respect to the trend of the shallow events. Finally, the P-axis trends of the 36 mechanisms for aftershocks in the depth range of the mainshock rupture (6-8 km), all in the main cluster, are approximately N85˚E to N120˚E, which includes the P-axis trend of the mainshock (N103˚E).

The aftershock hypocenter locations (Figure 2) suggest a single fault plane in the main cluster containing the mainshock rupture area and aftershocks. But the focal mechanisms indicate otherwise. The tabular volume contains earthquakes with distinctly different fault orientations. The majority of mechanisms are reverse, with sub-horizontal P-axis plunge. Significantly, the P-axis azimuths range over 90 degrees.

We performed stress inversions using the focal mechanisms (Figure 12). The data were split into different depth intervals to study potential depth variations of the local stress regime throughout the aftershock sequence. The package MSATSI (Martínez-Garzón *et al*., 2014) used in this study is based on the stress inversion algorithm SATSI developed by Hardebeck and Michael (2006), which is a damped inversion method that simultaneously inverts for the stress field orientations in subareas taking into account the adjacent subareas to smooth the solution, and provides a bootstrap re-sampling uncertainty assessment.

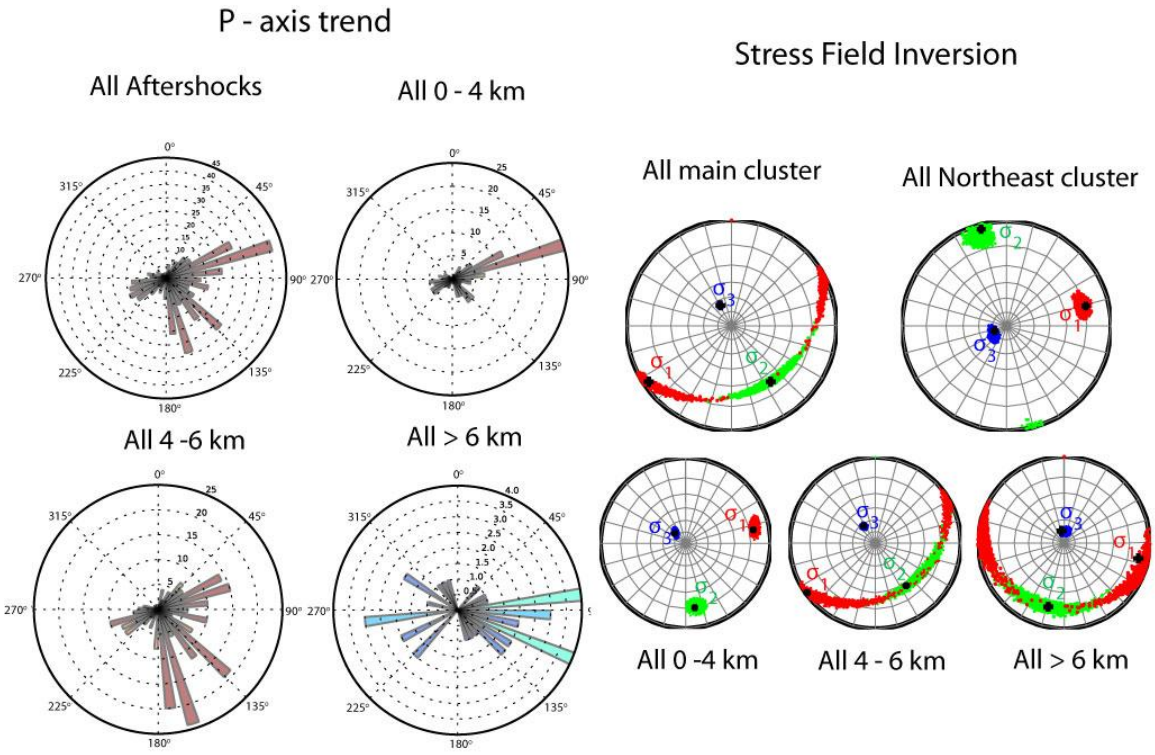

Figure 12. (left) Focal mechanism P-axis trend for various focal depth ranges. Note the tight N80E trend for shallow events, and more than 90 degree range for events in the 4-6 km depth range. The P-axis trend for shocks in the depth range of the mainshock rupture (> 6 km) exhibit P-axis trend of approximately N100E, consistent with the mainshock. (Right) stress field inverted from the focal mechanisms. The northeastern cluster events are shallow (less than 5 km) and along with shallow events in the main cluster invert for a well-constrained N80E subhorizontal max. compressive stress. The inversion for deeper events indicates a reverse fault environment, but the trend of maximum compressive stress is not well-resolved. This reflects the diversity of focal mechanisms in the 4-6 depth range in the main aftershock cluster.

Individual stress inversions were done for the main cluster and the northeastern aftershocks. The results suggest, at first glance, a difference between those two groups of aftershocks. Using all 358 events in the main cluster, the stress inversion best-estimate azimuth for the maximum principle stress (σ_1) is N55˚E (N235˚E) with sub-horizontal plunge. The 95% confidence region for the azimuths of σ_1 and σ_2 in the main cluster is large, approximately 70 degrees, whereas the near-vertical orientation of σ_3 is well constrained. This reflects the diversity of focal mechanisms in the main cluster. In contrast, the inversion result of 35 events in the northeastern cluster shows a well-constrained N75˚E-trending σ_1 with a shallow plunge of 15 degrees. Thus, the best-estimate orientation of the stress field for the northeastern aftershocks appears to be rotated approximately 20 degrees clockwise from the best estimate of the stress regime orientation using all shocks in the main cluster. However, most of the northeastern events are shallow (less than 5 km) whereas the main cluster is comprised mostly of deeper events, and the focal mechanisms in the main cluster show variability with depth (Fig. 10).

The events in the main cluster were divided into 3 different depth ranges (Fig. 12). For 94 focal mechanism solutions at depths less than 4 km, the stress inversion returned an ~N80˚E-trending sub-horizontal maximum principal stress (σ_1) and a nearly vertical σ3, which is in good agreement with the P-axis trends. The stress inversion of 228 events between 4 and 6 km depth resulted in a sub-horizontal σ_1 with an azimuth of N235˚E (N55˚E). The best fit σ_1 direction for events deeper than 6 km, although not well constrained with only 36 events, is sub-horizontal with a trend of ~N100˚E, which agrees with the P-axis azimuth of the mainshock focal mechanism (Herrmann, 2011).

The derived stress orientation of the shallow (< 4.0 km) events in the main cluster is very similar to that derived from the northeastern aftershocks. The apparent stress rotation mentioned above is not between the main cluster and the northeastern aftershocks, but occurs within the main cluster. A clockwise rotation of the inverted stress field occurs within the depth range 4 to 6 km where most of the main cluster aftershocks are located. The best-estimate azimuth of the sub-horizontal maximum compressive stress (σ_1) changes from N80˚E at shallow depth to N100˚E at the depth of the mainshock (8 km, approximately). The 4-6 km depth range shows a large (90 degree) range of focal mechanism P-axis trend and the density of aftershocks in this depth range suggests that it may mark the shallow limit of significant mainshock slip.

It is important to recognize that the inferences made here about the stress field are indirect, being based entirely on observations of the aftershock focal mechanisms (strain events), but the evidence suggests that the mainshock strongly altered the pre-existing stress field in the vicinity of the fault rupture in a way that promoted slip on planes with a variety of orientations.

Coulomb Stress Transfer Analysis

To better understand the aftershock distribution and the complexity of focal mechanisms and stress field, we investigated the static stress interaction between the mainshock and aftershocks by applying a Coulomb stress transfer analysis. Most investigations of Coulomb stress triggering have found that static stress change plays an important role in the production of aftershocks (King et al., 1994; Harris, 1998; Stein, 1999; Freed, 2005; Toda *et al*., 2011a). It has been demonstrated that positive changes of Coulomb stress as small as 0.1 bar (0.01 MPa) appear to be sufficient to trigger earthquakes (Stein, 1999).

We made two sets of Coulomb stress calculations using program Coulomb 3.3 (Toda et al., 2011b). We first calculated Coulomb stress change on specified representative receiver faults. This approach allows us to graphically examine the 3-dimensional spatial geometry of the Coulomb stress field and compare it with the aftershock hypocenter distribution. In the second approach, we take advantage of the nearly 400 focal mechanism solutions and compute the Coulomb stress change on each nodal plane, and then examine the statistics of nodal planes with positive stress change and their spatial location. The same slip model (displacement on the source fault) was used in both cases. According to Chapman (2013), the mainshock was a temporally and spatially complex rupture, comprised of 3 distinct subevents within a relatively small area. Motazedian and Ma (2014) derived similar results. The slip model used here for the source fault was based on the location and moment of the three subevents modeled by Chapman (2013), which is comparable to the finite fault slip model inverted from teleseismic waveforms by Hartzell *et al*. (2013).

Our focal mechanism solutions indicate that the aftershocks occurred on sets of fault planes with different orientations. Therefore, we cannot assume that the receiver faults have the same strike, dip and rake as the mainshock. We defined 3 different categories of receiver faults

based on the stress inversion results for different depth ranges: (1) 0 - 4 km: strike: N340˚E, dip: 60˚, rake: 90˚; (2) 4 - 6 km: strike: N325˚E, dip: 50˚, rake: 90˚; (3) > 6 km: strike: N30˚E, dip: 50˚, rake: 110˚. Those three mechanisms are taken as representative of the events in each depth range. Calculations were made in an elastic half-space using the Coulomb 3.3 program (Toda *et al.*, 2011b) with Young's modulus equal to 8×10^5 bar (8×10^4 MPa), shear modulus equal to 3.2×10^5 bar (3.2×10^4 MPa), and Poisson's ratio equal to 0.25.

Figure 13 shows in map view Coulomb stress change at 2 km depth on the category 1 receiver fault representing the shallow aftershocks in the main cluster and events in the northeastern group. The epicenters of earthquakes in the 0 - 4 km depth range are also plotted in Figure 13. The epicenters of the shallow earthquakes correlate well with the two zones of positive Coulomb stress change at 2 km depth. This is further illustrated in Figures 13 by vertical profiles through the center of the main aftershock cluster and through the center of the northeastern aftershock group. The respective profiles show contoured Coulomb stress change and projected aftershock hypocenters lying within a 10 km wide band centered on the two profiles, and clearly indicate that lobes of positive stress change correspond to the aftershock zones. Significantly, the good match for the northeastern aftershocks indicates that the very small stress transfer imparted by the mainshock promoted failure in this zone on fault planes with orientation very different from the mainshock rupture. The Coulomb stress calculations on receiver fault categories 2 and 3 show similar strong correlations of Coulomb stress change with the spatial distribution of aftershocks at depths between 4 and 6 km, and greater than 6 km, respectively . Considering the uncertainties in aftershock locations and details of the mainshock slip model, we expect to see some aftershocks located in the negative Coulomb stress change zones; however, there are relatively few examples of such.

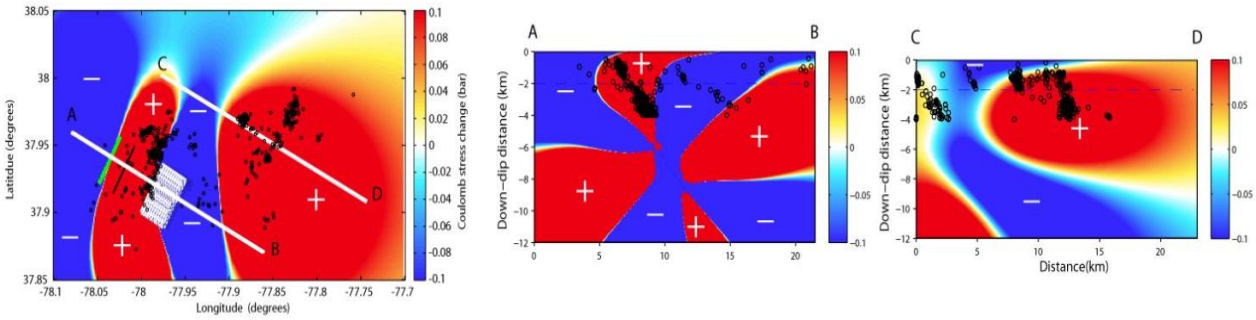

Figure 13. Contoured values of Coulomb stress change at 2 km depth resolved on receiver fault strike: 340, dip: 60, and rake: 90. The epicenters of aftershocks that occurred in the depth range 0 – 4 km are shown as small open circles. The projection of the source fault is shown by the rectangular grid. (Center and left) show contoured Coulomb stress change on vertical profiles A-B and C-D, with hypocenters projected to the profile from a 10 km wide band. The plus and minus signs indicate lobes of positive and negative Coulomb stress change, respectively. Note that the NW striking, NE dipping faults at shallow depth in the mainshock cluster and in the northeast cluster BOTH experience positive Coulomb stress change due to the mainshock.

A stricter calculation can be made to investigate whether the nodal planes of the aftershocks are promoted for failure by the Coulomb stress change. By resolving the Coulomb stress change on aftershock nodal planes in their rake directions, one need not make any assumptions about the receiver fault geometry. But while the shear stress on the two orthogonal

nodal planes is the same, the unclamping stress is different. So, except for the special case of zero fault friction, the Coulomb stress imparted to the two nodal planes will differ, and, except under unusual circumstances, we do not know which of the two planes slipped (Toda *et al*., 2011a). Because of the nodal plane ambiguity, we resolved the Coulomb stress change on both nodal planes of all 393 focal mechanisms. If we randomly select one of two nodal planes for each focal mechanism solution, 308 out of 393 events (78%) have positive stress change, and the percentage of stress increase for events in the main cluster and the northeastern cluster are 80% (286 of 358) and 63% (22 of 35) respectively. A percentage of 87% (343 out of 393) were found to have been brought closer to failure if we select the larger change from each pair of nodal planes, including 312 out of 358 (87%) for the main cluster and 31 out of 35 (89%) for the northeastern aftershocks. Figure 14 shows the results derived by choosing the larger Coulomb stress change from each pair of nodal planes. The majority of earthquakes in the northeastern group of aftershocks show small positive Coulomb stress change of approximately 0.2 bar (0.02 MPa). A further observation concerning these northeastern aftershocks is that 21 out of the 35 focal mechanisms show a positive stress change on the N-NW striking, NE-dipping nodal plane, whereas the other nodal plane shows in most cases negative stress change. This indicates that the faulting probably occurred on the NW-striking, NE-dipping planes, consistent with the geometry of the hypocenter locations (Figure 2).

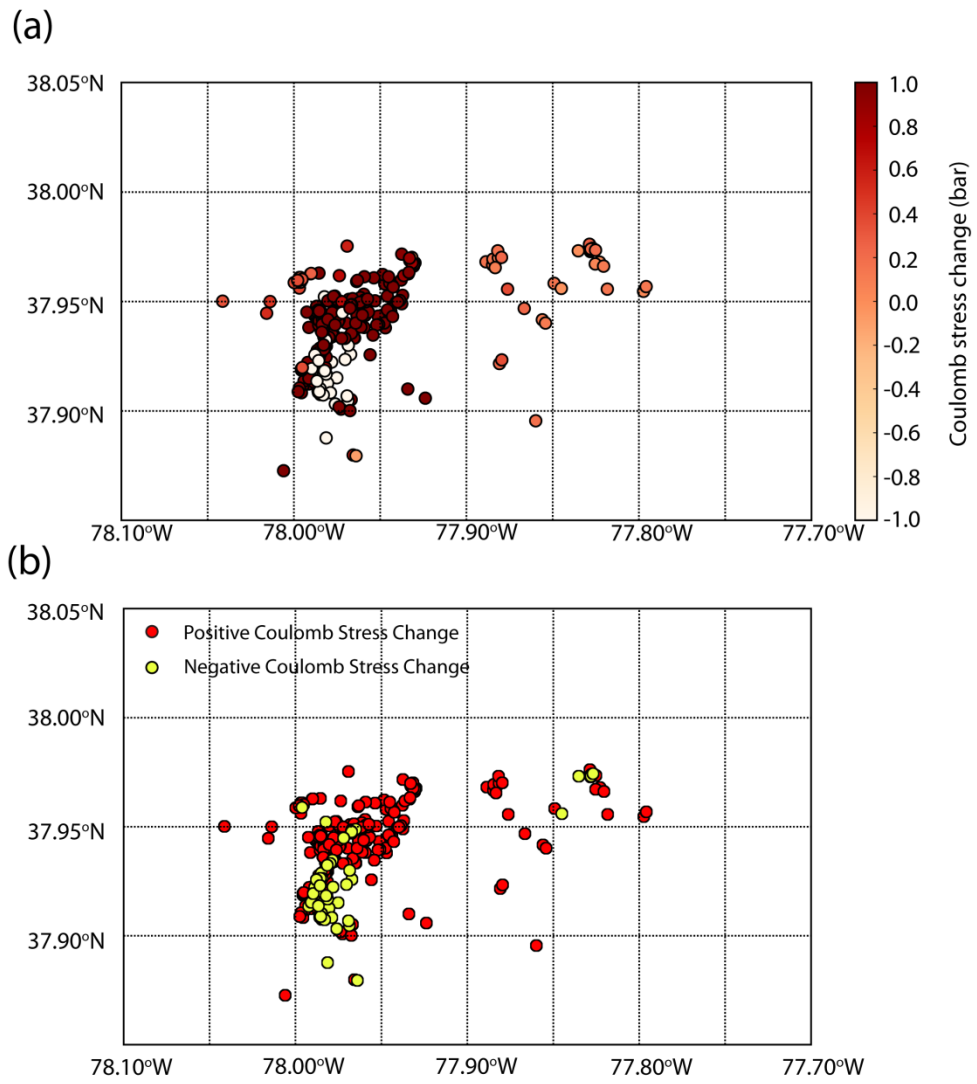

Figure 14. Coulomb stress change resolved on focal mechanism nodal planes. (a) Selection of the most positive Coulomb stress change value from each pair of nodal planes: positive stress change percentage is 87.3% (343 events). (b) Selection of the most positive Coulomb stress change value from each pair of nodal planes: symbols show positive and negative values. Note that $\mu' = 0.8$.

Moment Tensor Inversion

Focal mechanisms were determined for 59 aftershocks in the main aftershock cluster using the moment tensor inversion method of Ebel and Bonjer (1990). First-motion amplitudes and polarities were read from the direct P waves at stations surrounding the event. S waves were rotated so that the amplitudes from the transverse components of the direct S waves could be read (SV waves were past the critical angle at the surface and so could not be used in the analysis). The instrument gains were used to convert the P and SH amplitudes to ground motions. The ground-motion amplitude data were input into a linear least-squares inversion to calculate the five independent components of a traceless moment tensor that best predicts the

observed amplitudes and polarities. The resulting moment tensor was decomposed into the largest possible double-couple moment tensor and a residual compensated linear vector dipole (CLVD) moment tensor. The source moment, strike, dip, and rake were calculated from the double-couple. An additional non-linear least-squares inversion code was used to find seismic moment, strike, dip, and rake values that optimize the fit between the observed amplitudes and those calculated from the double-couple solution.

This method was only appropriate for small magnitude events due to the assumption that the source time function (STF) is so short in duration that it can be represented by a Dirac delta function (Ebel and Bonjer, 1990). Some other assumptions and limitations are part of the application of this moment tensor inversion method (Ebel and Bonjer, 1990). The seismic velocity structure between all sources and receivers was assumed to be the same for all events, and anelastic attenuation was assumed to be so small that it could be ignored in the analysis. All stations were located at far-field distances from the source, and only direct body waves were used in the moment tensor inversions to avoid distortion from reflected and refracted waveforms.

The seismic network data and velocity model used for the relative location analysis were also used in the moment tensor analysis. Focal mechanisms were determined for events that had been relocated using the relative location method so that nodal plane orientations of the focal mechanisms could be compared with trends in the seismicity near the aftershock locations.

Many independent tests were conducted to determine accurate focal mechanisms using the moment tensor inversion method. Initially, inversions using only P-wave first-motion amplitudes were performed because the initial P-wave amplitudes were relatively easy to identify on many of the station seismograms. S-wave first arrivals can be masked by scattered P-waves and P-to-S wave conversions, making a clear S-wave first arrival difficult to determine (Ebel and Bonjer, 1990). Thus, as a first step in the focal mechanism procedure, P-wave only inversions using first-motion amplitudes read from common stations for events with small offsets in hypocentral locations were performed, and the resulting focal mechanisms were compared to determine if the different events had similar double couple solutions (Figure 15). S-wave first-motion amplitudes at common stations were then included in the inversion to determine whether the focal mechanisms found using both P- and S-wave amplitudes were similar to the focal mechanism solutions using only P waves for the same events (Figure 15). S-wave first arrivals at stations closer than 3 km from the hypocenter were not used because the uncertainty in the hypocentral location can lead to large uncertainties in the rotation of the horizontal components to SV and SH ground motions. Also, small shifts in the hypocentral location could result in large changes in station take-off angle on the SH-wave radiation pattern. In many cases, the addition of the S-wave amplitudes caused little change in the focal mechanisms relative to the P-wave only inversion, or they caused a rotation of the nodal planes relative to the P-only solution that was consistent among all events with nearby hypocenters (Figure 15). Additional body-wave amplitude picks at stations that were not common among the events with small offsets in hypocentral locations were then included in the inversion to further test the calculated focal mechanisms. The most accurate focal mechanisms are those that had little change in inversion results when independent data were included with common P- and S-wave stations, for which the RMS error between calculated and observed amplitudes was minimized, and for which the CLVD component was less than 1/6 of the seismic moment.

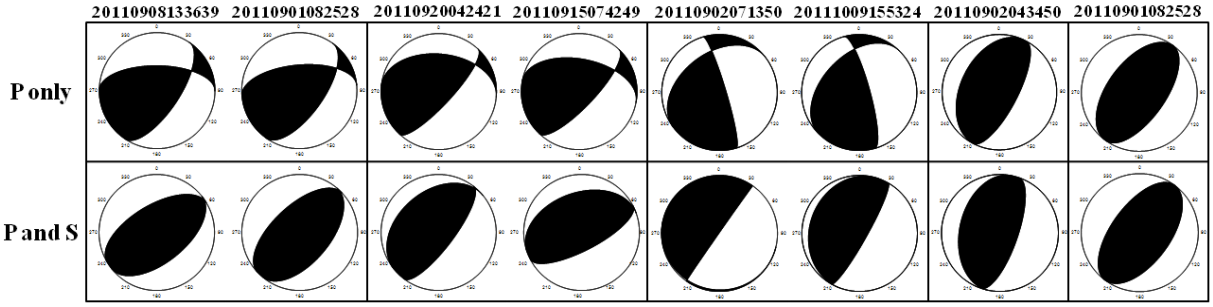

Figure 15. Focal mechanism analysis for pairs of events with small hypocentral differences determined from the relative location analyses. The two events on the right show examples of focal mechanisms that experienced little to no change from P-wave only to P- and S-wave inversion results. The number above each column of focal mechanisms shows the year, month day, hour, minute and second of the origin time of the event.

Fifty-nine focal mechanisms were created using the moment tensor inversion method for events that had been relocated using the relative location method (Figures 11 and 12). Accurate focal mechanisms were created for events with hypocentral depths ranging from 2.45 km to 8.00 km and moment magnitudes ranging from 0.48 to 2.69. Uncertainties in the calculated strikes and rakes of the focal mechanisms in this study range from ±0.01º to ±6.35º whereas uncertainties in the calculated dips range from ±0.01º to ±1.61º. Focal mechanisms calculated for events on the two primary fault planes of the main fault structure generally depict thrust fault motion and have a nodal plane that corresponds closely with the fault planes delineated by the relative location hypocenters (Figures 11 and 12). Instances of normal fault motion on planes with similar strikes and dips as nearby thrust focal mechanisms were calculated for two events on the main fault structure (Figures 11 and 12). In addition, normal faulting also occurred for several events that were located about 1-2 km northwest of the main aftershock zone (Figure 12). These events are located in the footwall block northwest of the main fault, and they seem to occur on a shallow planar feature and have similar strikes and dips as nearby thrust events on the main fault.

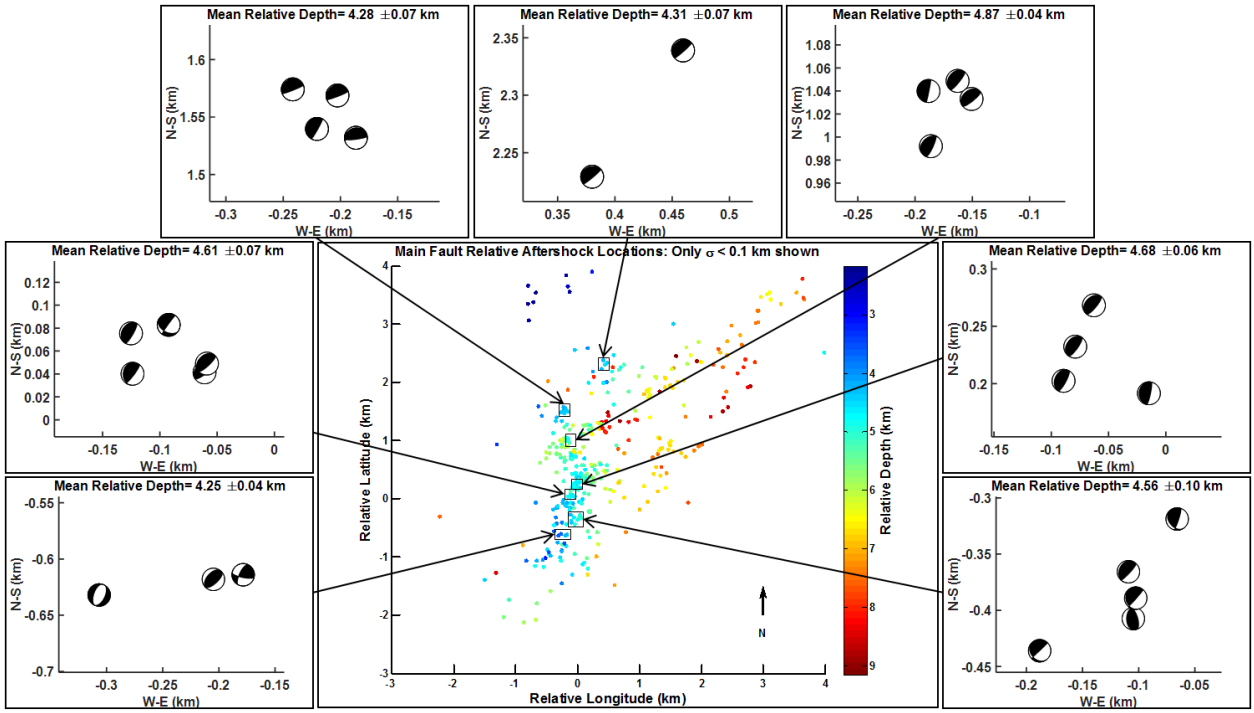

Figure 16. Map view of relative aftershock epicenters colored by depth. Clusters of aftershocks with small hypocentral distances are shown. Focal mechanisms calculated by the inversion of the source moment tensor are represented in map view. The focal mechanism plots in this figure all have the same vertical and horizontal scale to show relative epicentral distances, and the mean relative depth of the hypocenters is displayed above each plot. Focal mechanism solutions were compared to the trend of the aftershock hypocenters to determine which nodal plane is the probable fault plane. Focal mechanisms for the southern aftershocks depict a northeast striking fault dipping steeply to the southeast. Aftershock focal mechanisms show an increase in strike azimuth at more northern locations on the fault structure. The large majority of the aftershock focal mechanisms depict reverse fault motion.

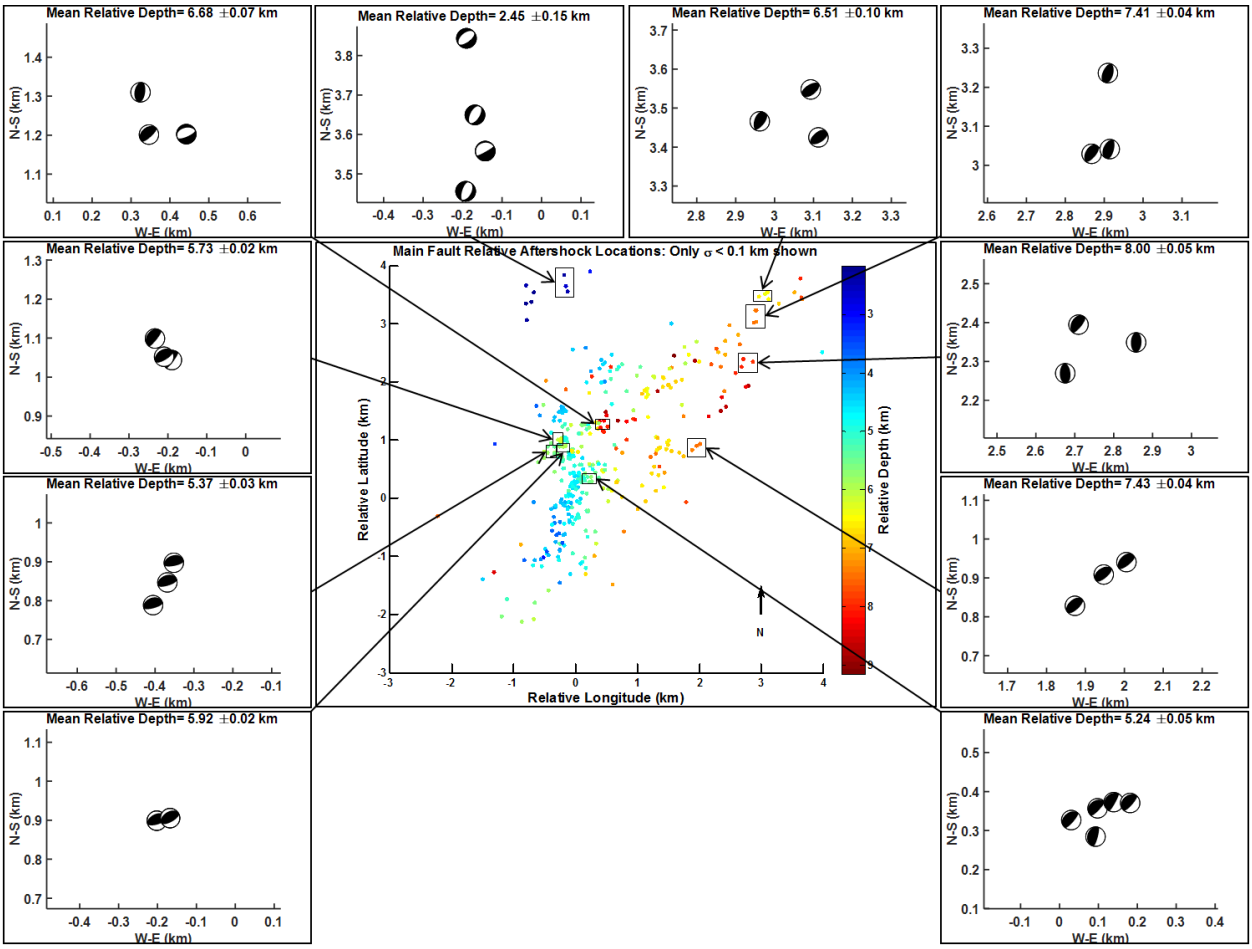

Figure 17. Map view of relative aftershock epicenters colored by depth. Clusters of aftershocks with small hypocentral distances are delineated by boxes. Focal mechanisms calculated by the inversion of the source moment tensor are represented in map view. The focal mechanism plots in this figure all have the same vertical and horizontal scale to show relative epicentral distances and the mean relative depth of the hypocenters within that box is displayed above each plot. Focal mechanism solutions were compared to the trend of aftershock hypocenters to determine which nodal plane is the probable fault plane**.** Aftershock focal mechanisms show a slight decrease in dip at deeper locations on the fault structure. Focal mechanisms located at a relative latitude of 1 km depict east-west trending features and are located at the juncture of two different striking and offset planar features. Deeper aftershocks show a northeast trending fault with reverse fault motion. The shallow cluster of aftershocks shown at the top of the figure depict normal faulting with similar strikes and dips as other focal mechanisms with deeper hypocenters. This shallow cluster is slightly offset to the northwest from the projected fault plane calculated from the deeper events. The offset locations of this shallow cluster help explain the difference in fault motion compared to the primarily reverse thrust trend in the primary aftershock zone.

The moment tensor inversion method of Ebel and Bonjer (1990) and relative location method of Ebel et al. (2008) define a complicated set of fault structures that consist of two primary planes (Q1 and Q2), one smaller planar feature (Q3), along with some off-fault

seismicity near the intersection of planes Q1 and Q2 (Figures 8 and 9). Planes Q1, Q2, and Q3 are all part of the Quail fault zone named by Horton et al. (2012a, 2012b) (Figure 1). The seismicity of the northernmost primary fault plane (Q1) has a strike and dip of 045º/67º, whereas Q2 has a strike and dip of 002º/72º. Q3 has a strike and dip of 056º/58º, striking northeast similar to Q1 but with a shallower dipping plane. Results of the moment tensor inversion for events on the southern primary fault plane (Q2) show focal mechanisms with one of their nodal planes with similar strikes and dips to the trend in seismicity as imaged in the relative location analysis (Figure 16). Focal mechanisms calculated for events on Q1 also have one set of nodal planes similar to the strike and dip of the local trend in the seismicity as determined by the relative location analysis (Figure 17). Fault motion on Q1 and Q2 is primarily pure thrust with a few instances of normal faulting (Figures 16 and 17). The shallow cluster of events offset about 1-2 km to the northwest of the main fault illuminate a small planar fracture with strike and dip that is similar to the main fault, but this northwestern seismicity cluster seems to have experienced normal fault motion in the month following the mainshock (Figure 17).

Discussion and Conclusions

This study of the aftershock sequence of the M_w 5.7, August 23, 2011 Mineral, Virginia, earthquake resolved spatial details within the previously recognized tabular main aftershock zone and gave us some insights concerning the stress field operative during, and perhaps prior to, the early phase of the aftershock sequence.

The main aftershock cluster is approximately 1 km thick and exhibits gross strike and dip in agreement with the mainshock fault plane. The majority of the focal mechanisms are of reverse type. However, the near-planar arrangement of the aftershocks in the main cluster belies the fact that the majority of them exhibit nodal planes with orientations significantly different from the mainshock. An important observation is the fact that this variability of the main cluster focal mechanisms is not random, but depends on the location of the aftershocks with respect to the mainshock. Shallow shocks mostly exhibit north-northwest trending nodal planes and invert to yield a well-constrained best-estimate maximum principle stress direction that is sub-horizontal, trending approximately N80°E. But most of the main cluster aftershocks occurred in the depth range 4 to 6 km. In contrast to the shallower shocks, those mostly reverse events show a 90 degree range of nodal plane trend, from approximately N-S to E-W.

Relative event location using master events define a complicated set of fault structures within the main aftershock cluster. The large variability of focal mechanism P-axis trend in the 4-6 km depth range results in large uncertainty in the stress field inversion for that depth interval which contains by far the majority of main cluster events: the best estimate for the maximum principle stress direction for that depth range is sub-horizontal and trends N55°E, but the trend is uncertain by approximately 70 degrees at the 95% confidence level. The 25 degree difference in σ_1 azimuth found for the events in the 4-6 km depth range and that found for the shallower aftershocks is clearly insignificant given the uncertainties.

The locations of the aftershocks and their focal mechanisms in the depth range 4-6 km in the main aftershock cluster point to the role of static and possibly dynamic stress changes near the mainshock fault rupture. The location of the events in a rough quarter-circle, up-dip and to the northeast of the rupture zone, reflects the direction of mainshock rupture propagation. The concentration of aftershocks and the diversity of their nodal plane orientations within this aftershock halo is likely because positive static Coulomb stress changes are largest just outside

the zone of fault rupture, thus promoting rupture on other faults that are less than optimally oriented in the ambient stress field. The location of the aftershocks in the direction of forward directivity may possibly be due to lingering effects of dynamic stresses operative during fault rupture and elastic wave propagation. Perhaps poroelastic effects in a permeable solid with pore fluids persist long after the seismic waves have passed.

The possibility of a strongly depth-dependent ambient stress field prior to the Mineral mainshock has some interesting implications. If in fact that was the case, the mainshock rupture may have been confined to depths greater than approximately 6 km by the change in the resolved shear stress on the plane containing the rupture.

References

Allen, R. (1982). Automatic phase pickers: their present use and future prospects, *Bull. Seismol. Soc. Am.* **72**, S225–S242.

Bollinger, G.A., (1969). Seismicity of the central Appalachian states of Virginia, West Virginia, and Maryland - 1758 through 1968, *Bull. Seismol. Soc. Am.*, 59, 2103-2111.

Bollinger, G.A. (1973a). Seismicity and crustal uplift in the southeastern United States, *Am. J. Sci*., 273-A, 396-408.

Bollinger, G.A. (1973b). Seismicity of the southeastern United States, *Bull. Seismol. Soc. Am.*, 63, 1785-1808.

Bollinger, G.A., M.C. Chapman and T.P. Moore (1980). Central Virginia regional seismic network: Crustal structure in central and southwestern Virginia, NUREG/CR-1217, U.S. Nuclear Regulatory Commission, Washington, D.C., 187 p.

Bollinger, G.A, A.C. Johnston, P. Talwani, L.T. Long, K.M. Shedlock, M.S. Sibol and M.C. Chapman (1991). Seismicity of the southeastern United States; 1698 to 1986, in Neotechtonics of North America, D.B. Slemmons, E.R. Engdahl, M.D. Zoback, and D.D. Blackwell (Editors), Geological Society of America, 291-308.

Chapman, M.C. (2015). Magnitude, recurrence interval, and near-source ground-motion modeling of the Mineral, Virginia, earthquake of 23 August 2011, in *The 2011 Mineral, Virginia, Earthquake and its Significance for Seismic Hazards in Eastern North America*, Horton, J.W., Jr., Chapman, M.C., and Green, R.A., (Editors), Geological Society of America Special Paper 509, doi:10.1130/2015.2509(02), 27-45.

Chapman, M.C., (2013). On the Rupture Process of the 23 August 2011 Virginia Earthquake: *Bulletin of the Seismological Society of America*, v. 103, no. 2A, 613-628.

Coruh, C., Bollinger, G.A., and Costain, J.K., (1988). Seismogenic structures in the central Virginia seismic zone: *Geology*, v. 16, 748-751.

Dicken, C. L., Nicholson, S. W., Horton, J. D., Kinney, S. A., Gunther, G., Foose, M. P., and Mueller, J. A. L., (2005). Integrated Geologic Map Databases for the United States: Delaware, Maryland, New York, Pennsylvania, and Virginia: U.S. Geological Survey Open-File Report 2005-1325, U.S. Geological Survey, Reston, VA.

Ebel, J.E. and Bonjer, K.-P., (1990). Moment tensor inversion of small earthquakes in southwestern Germany for the fault plane solution: *Geophysical Journal International*, v. 101, 133-146.

Ebel, J.E., Moulis, A.M., Smith, D., and Hagerty, M., (2008). The 2006-2007 Earthquake Sequence at Bar Harbor, Maine: *Seismological Research Letters*, v. 79, no. 3, 457-468.

Freed, A. M. (2012). Earthquakes: Casting stress shadows, *Nature* **5**, 371–372.

Freed, A. M. (2005). Earthquake triggering by static, dynamic, and postseismic stress transfer, *Ann. Rev. Earth Planet. Sci.* **33**, 335–367.

Hardebeck, J. L., and A. J. Michael (2006). Damped regional-scale stress inversions: Methodology and examples for southern California and the Coalinga aftershock sequence, *J. Geophys. Res.*, Solid Earth **111**, no. B11, B11310, doi 10.1029/2005JB004144.

Harris, R. A. (1998). Introduction to special section; stress triggers, stress shadows, and implications for seismic hazard, *J. Geophys. Res.* **103**, 24,347–24,358.

Hartzell, S., C. Mendoza, and Y. Zeng (2013). Rupture model of the 2011 Virginia, earthquake from teleseismic and regional waveforms, *Geophys. Res. Lett.* **40**, 5665–5670.

Heller, M.J. and A.M. Carter (2015). Residential property damage in the epicentral area of the Mineral, Virginia, earthquake of 23 August 2011, in *The 2011 Mineral, Virginia, Earthquake and its Significance for Seismic Hazards in Eastern North America*, Horton, J.W., Jr., Chapman, M.C., and Green, R.A., (Editors), Geological Society of America Special Paper 509, doi:10.1130/2015.2509(10), 173-187.

Herrmann, R.B. (2011). St. Louis University Earthquake Center website: http://www.eas.slu.edu/eqc/eqc20110823.html (last accessed January, 2015).

Horton, J.W., Jr., Chapman, M.C., Carter, A.M., Carter, M.W, Harrison, R.W., Herrmann, R.B., and Snyder, S.L., (2012a). Faults delineated by aftershocks associated with the 2011 central Virginia earthquake and their tectonic setting: Geological Society of America Abstracts with Programs, v. 44, no. 4, 14.

Horton, J.W., Jr., McNamara, D.E., Shah, A.K., Gilmer, A.K., Carter, A.M., Burton, W.C., Harrison, R.W., Carter, M.W., Herrmann, R.B., and Snyder, S.L., (2012b). Preliminary analysis of magnitude 5.8 Virginia earthquake causative fault and subsidiary faults illuminated by aftershocks: Geological Society of America Abstracts with Programs, v. 44, no. 7, 381.

King, G., R. S. Stein, and J. Lin (1994). Static stress changes and the triggering of earthquakes, *Bull. Seismol. Soc. Am.* **84**, 935–953.

Kim, W.-Y., and Chapman, M., (2005). The 9 December 2003 Central Virginia Earthquake Sequence: A Compound Earthquake in the Central Virginia Seismic Zone: *Bulletin of the Seismological Society of America*, v. 95, no. 6, 2428-2445.

Lahr, J. C. (1999). HYPOELLIPSE: A computer program for determining local earthquake hypocentral parameters, magnitude, and first-motion pattern, U.S. Geol. Surv. Open-File Rept. 99-23, version 1.1, 119 pp., software, available at http://pubs.usgs.gov/of/1999/ofr-99-0023/ (last accessed December, 2014).

Martínez-Garzón, P., Kwiatek, G., Ickrath, M. and M. Bohnhoff (2014). MSATSI: A MATLAB package for stress inversion combining solid classic methodology, a new simplified user-handling and a visualization tool, *Seismol. Res. Lett.* **85**, 4, doi: 10.1785/0220130189, 896-904.

McNamara, D. E., Benz, H. M., Herrmann, R. B., Bergman, E. A., Earle, P., Meltzer, A., Withers, M., and M. Chapman (2014). The M_w 5.8 Mineral, Virginia, earthquake of August 2011 and aftershock sequence: constraints on earthquake source parameters and fault geometry, *Bull. Seismol. Soc. Am.* **104**, 40–54.

Motazedian D., S. Ma (2014). A review study of the source parameters of the August 2011 M_w 5.7 Virginia earthquake, *Bull. Seismol. Soc. Am.* **104**, no. 5, 2611–2618.

Pratt, T.L., C. Coruh, J.K. Costain, and L. Glover III (1988). A geophysical study of the Earth's crust in central Virginia: Implications for Appalachian crustal structure, *J. Geophys. Res.* 93, 6649-6667.

Pratt, T.L., Horton, J.W., Jr., Spears, D.B., Gilmer, A.K., and McNamara, D.E., (2015). The 2011 Virginia Mw 5.8 earthquake: Insights from seismic reflection imaging into the influence of older structures on eastern U.S. seismicity, *in* Horton, J.W., Jr., Chapman, M.C., and Green, R.A., eds., The 2011 Mineral, Virginia, Earthquake, and Its Significance for Seismic Hazards in Eastern North America: Geological Society of America Special Paper 509, 285-294.

Snoke, J. A. (2009). FOCMEC: FOCal MEChanisms Determinations. Manual., http://ds.iris.edu/pub/programs/focmec/ (last accessed December 2014).

Snoke, J. A., J. W. Munsey, A. C. Teague, and G. A. Bollinger (1984). A program for focal mechanism determination by combined use of polarity and SV-P amplitude ratio data, *Earthq. Notes* **55**, no. 3, 15.

Stein, R. (1999). The role of stress transfer in earthquake occurrence, *Nature* **402**, 605–609.

Tabor, S. (1913). Earthquakes in Buckingham county, Virginia, *Bull. Seismol. Soc. Am.* 3, 124-133.

Toda, S., J. Lin, and R. S. Stein (2011a). Using the 2011 Mw 9.0 off the Pacific coast of Tohoku earthquake to test the Coulomb stress triggering hypothesis and to calculate faults brought closer to failure, *Earth Planets Space*, **63**, 725 – 730.

Toda, S., R. S. Stein, V. Sevilgen, and J. Lin (2011b). Coulomb 3.3 Graphic-Rich Deformation and Stress-Change Software for Earthquake, Tectonic, and Volcano Research and Teaching – User Guide, United States Geological Survey Open File Report 2011-1060, 63 p., available at http://pubs.usgs.gov/of/2011/1060/.

Waldhauser, F. (2001). HYPODD – A program to compute double-difference hypocenter locations, U.S. Geol. Surv. Open-File Rept. 01-113, 25 pp.

Waldhauser, F., and W. L. Ellsworth (2000). A double-difference earthquake location algorithm: Method and application to the northern Hayward fault, California, *Bull. Seismol. Soc. Am.* **90**, 1353–1368.

Wells, D., J.A. Egan, D.G. Murphy and T.P. Paret (2015). Ground shaking and structural response of the Washington Monument during the 2011 Mineral, Virginia, earthquake, in *The 2011 Mineral, Virginia, Earthquake and its Significance for Seismic Hazards in Eastern North America*, Horton, J.W., Jr., Chapman, M.C., and Green, R.A., (Editors), Geological Society of America Special Paper 509, doi:10.1130/2015.2509(12), 199-234.

Withers, M., R. Aster, C. Young, J. Beiriger, M. Harris, S. Moore, and J. Trujillo (1998). A comparison of selected trigger algorithms for automated global seismic phase and event detection, *Bull. Seismol. Soc. Am*. **88**, 95–106.

Wu, Q., M. C. Chapman, and J. N. Beale (2014). Automatic detection and hypocenter determination of the August 23, 2011 Mineral, Virginia, earthquake aftershock sequence, *Seismol. Res. Lett.* **85**, 241.

Zoback, M.L., (1992). First- and second-order patterns of stress in the lithosphere: The World Stress Map project. *J. Geophys. Res.* **97**, 11,703-11,728.